

Influence of Support Material on the Structural Evolution of Copper during Electrochemical CO₂ Reduction

Ezra S. Koh,^{*[a]} Simon Geiger,^[b] Alexander Gunnarson,^[c] Timo Imhof,^[a] Gregor M. Meyer,^[a] Paul Paciok,^[d] Bastian J. M. Etzold,^[a] Marcus Rose,^[a] Ferdi Schüth,^[c] and Marc Ledendecker^{*[a, e]}

The copper-catalyzed electrochemical CO₂ reduction reaction represents an elegant pathway to reduce CO₂ emissions while producing a wide range of valuable hydrocarbons. The selectivity for these products depends strongly on the structure and morphology of the copper catalyst. However, continued deactivation during catalysis alters the obtained product spectrum. In this work, we report on the stabilizing effect of three different carbon supports with unique pore structures. The influence of pore structure on stability and selectivity was examined by high-angle annular dark field scanning transmission electron microscopy and gas chromatography measure-

ments in a micro-flow cell. Supporting particles into confined space was found to increase the barrier for particle agglomeration during 20 h of chronopotentiometry measurements at 100 mA cm⁻² resembling long-term CO₂ reduction conditions. We propose a catalyst design preventing coalescence and agglomeration in harsh electrochemical reaction conditions, exemplarily demonstrated for the electrocatalytic CO₂ reduction. With this work, we provide important insights into the design of stable CO₂ electrocatalysts that can potentially be applied to a wide range of applications.

Introduction

Anthropogenic activities have led to increased carbon dioxide (CO₂) concentrations in the atmosphere currently reaching the highest levels recorded in human history.^[1] CO₂ capture and the electrochemical CO₂ reduction reaction (CO₂RR) provide a pathway to reduce CO₂ and simultaneously produce valuable chemical feedstock chemicals. Copper is the only element that

allows the electrochemical conversion of CO₂ into products requiring more than two electrons including many high-value-added chemicals such as methanol, ethylene, or ethanol.^[2–4] While various catalyst designs have been reported in recent years, the focus in research was mostly put on increasing the catalysts' activities and tuning the product spectrum.^[5–13] Despite impressive reported activities and selectivities, copper is highly susceptible to deactivation and restructuring under CO₂RR conditions.^[14–17] Huang et al. reported partial fragmentation of Cu nanocubes (CuNCs) by nanodeclustering followed by coalescence and agglomeration, resulting in large aggregates composed of CuNCs.^[18] Osowiecki et al. elucidated the time dependency of degradation.^[19] During the first hour of reaction, agglomeration/sintering was the predominant effect followed by continuous declustering, in which, after 24 h, several particles were smaller in size than the original Cu particles. They propose that common intermediates from the CO₂RR such as CO, cause the formation of enlarged cohesive copper nanoparticles (CuNPs), in contrast to reactions under argon, in which only agglomerates of smaller particles were formed. Popovic et al., as well as Vavra et al., proposed a two-step transient dissolution and redeposition mechanism responsible for the restructuring of CuNPs.^[14,15] While Vavra et al. observed changes in particle size suggesting an Ostwald ripening-type process, Popovic et al. demonstrated a fragmentation of larger CuNPs into smaller ones. Evidently, there is no clarity yet concerning the degradation mechanisms responsible for the deactivation. Taking into account that the product spectrum of the Cu-catalyzed electrochemical CO₂RR strongly depends on the structure and morphology of the catalyst, continuing catalyst reorganization hampers the establishment of clear correlations between the nature of the active sites and the observed product spectrum. In this work, we describe how carbon


[a] E. S. Koh, T. Imhof, G. M. Meyer, Prof. Dr. B. J. M. Etzold, Prof. Dr. M. Rose, Prof. Dr. M. Ledendecker
 Technical University of Darmstadt
 Department of Chemistry
 Ernst-Berl-Institut für Technische und Makromolekulare Chemie
 64287 Darmstadt, Germany
 E-mail: ezra.koh@tu-darmstadt.de


[b] Dr. S. Geiger
 Department of Technical Thermodynamics
 Deutsches Zentrum für Luft- und Raumfahrt, Stuttgart
 Pfaffenwaldring 38–40, 70569 Stuttgart

[c] A. Gunnarson, Prof. Dr. F. Schüth
 Department of Heterogeneous Catalysis
 Max Planck-Institut für Kohlenforschung
 45470 Mülheim an der Ruhr, Germany

[d] Dr. P. Paciok
 Ernst Ruska-Centre for Microscopy and Spectroscopy with Electrons and Peter Grünberg Institute
 Forschungszentrum Jülich GmbH
 52425 Jülich, Germany

[e] Prof. Dr. M. Ledendecker
 Current address: Technical University of Munich
 Department of Sustainable Energy Materials
 94315 Straubing
 E-mail: marc.ledendecker@tum.de

 Supporting information for this article is available on the WWW under <https://doi.org/10.1002/celec.202200924>

 © 2023 The Authors. ChemElectroChem published by Wiley-VCH GmbH. This is an open access article under the terms of the Creative Commons Attribution License, which permits use, distribution and reproduction in any medium, provided the original work is properly cited.

supports can stabilize copper nanoparticles by space confinement. We systematically support copper nanoparticles on three carbon supports with well-defined pore structures and morphologies. It is demonstrated how the carbon support significantly influences the reorganization of Cu nanoparticles during the electrochemical CO₂RR and we propose pore-confinement as an efficient measure to circumvent agglomeration. By and large, we provide important insights into the design of stable electrocatalysts for electrochemical CO₂ reduction.

Results and Discussion

To determine the stabilizing effect of the support, we employed three distinct carbon materials, namely, Vulcan XC 72R (Vul), Ketjenblack EC-300 J (KB), and mesoporous graphitic spheres (MGS) (Figure 1a). First, the microstructure of Vul, KB, and MGS was investigated by N₂-physisorption displaying considerable differences in their structural properties (Figure 1b). The pore size distributions were determined through fitting density functional theory (DFT) models for carbon materials with the least deviation from experimental data and are shown with the measured particle size distribution (Figure 1d–f, c.f. Supporting Information).^[20] All carbon support surface areas were quantified by Brunauer-Emmet-Teller (BET) analysis. Regarding the limitations of BET on micropore-containing materials see the supporting information.

The type II isotherm of Vulcan indicates the nonporous nature of the carbon material.^[21] The BET analysis reveals an apparent specific surface area (SSA) of 230 m²g⁻¹. Additionally, the DFT analysis shows a limited number of micropores with a

pore volume of 0.26 mLg⁻¹ (Figure 1d). The isotherm of the Ketjenblack material resembles an H4 hysteresis loop which is found in micro-mesoporous carbon materials.^[21] This is in line with the DFT calculated pore size distribution (Figure 1e). Ketjenblack possesses an apparent SSA of 730 m²g⁻¹ alongside significant porosity with a pore volume of 0.75 mLg⁻¹. As the third support material, we synthesized mesoporous graphitic spheres with an apparent SSA of 2000 m²g⁻¹ and 2 mLg⁻¹ in pore volume. The employed hard-templating method allows for precise control of the pore form and size distribution with high reproducibility.^[22] The type IVa isotherm and H1-like hysteresis loop indicate a carbon material with a defined, ink-bottle-shaped mesopore network. The adsorption up to a p/p₀ of 0.5 corresponds to the pore filling of mesopores in the size range of 3 to 6 nm as shown in the DFT adsorption pore size distribution in Figure 1f. All carbons feature the same adsorption characteristics at high relative pressures of >0.95 p/p₀, attributed to macropore filling. For the defined MGS support, this consists of interparticle void spaces, while for the KB and Vul supports, this additionally includes the filling of intraparticle hollow spaces. After having established the three distinct support materials, copper nanoparticles were deposited by incipient wetness impregnation on KB (Cu@KB) and MGS (Cu@MGS) as well as by deposition of pre-formed copper nanoparticles on Vul (Cu@Vul). To obtain information on the phase composition of the synthesized materials, powder X-ray diffraction was carried out.

For Cu@MGS and Cu@KB, the characteristic reflections of Cu₂O with the respective 111 planes at 2θ = 36.5° are visible as a broad reflex, indicating very small crystallite sizes. This is in line with literature where bare CuNPs oxidize to Cu₂O in contact

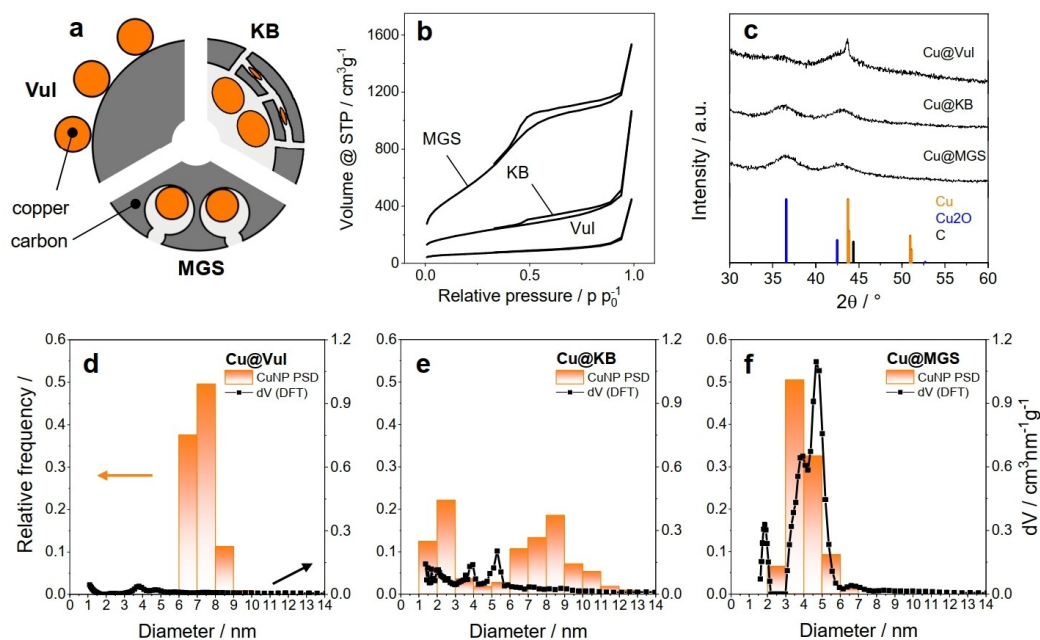


Figure 1. (a) Schematic depiction of Cu nanoparticles incorporation into mesoporous graphitic spheres, Ketjenblack and Vulcan. (b) Experimental nitrogen (77.4 K) adsorption and desorption isotherms of bare MGS, KB, and Vul. (c) X-ray diffractogram of the three catalyst systems with Cu (PDF 00-004-0836), Cu₂O (PDF 04-007-9767), and C (PDF 75-1621) references. DFT calculated pore size (black) and measured particle size distribution (orange bars, Figure S1–S3) of (d) Cu@Vul, (e) Cu@KB, and (f) Cu@MGS.

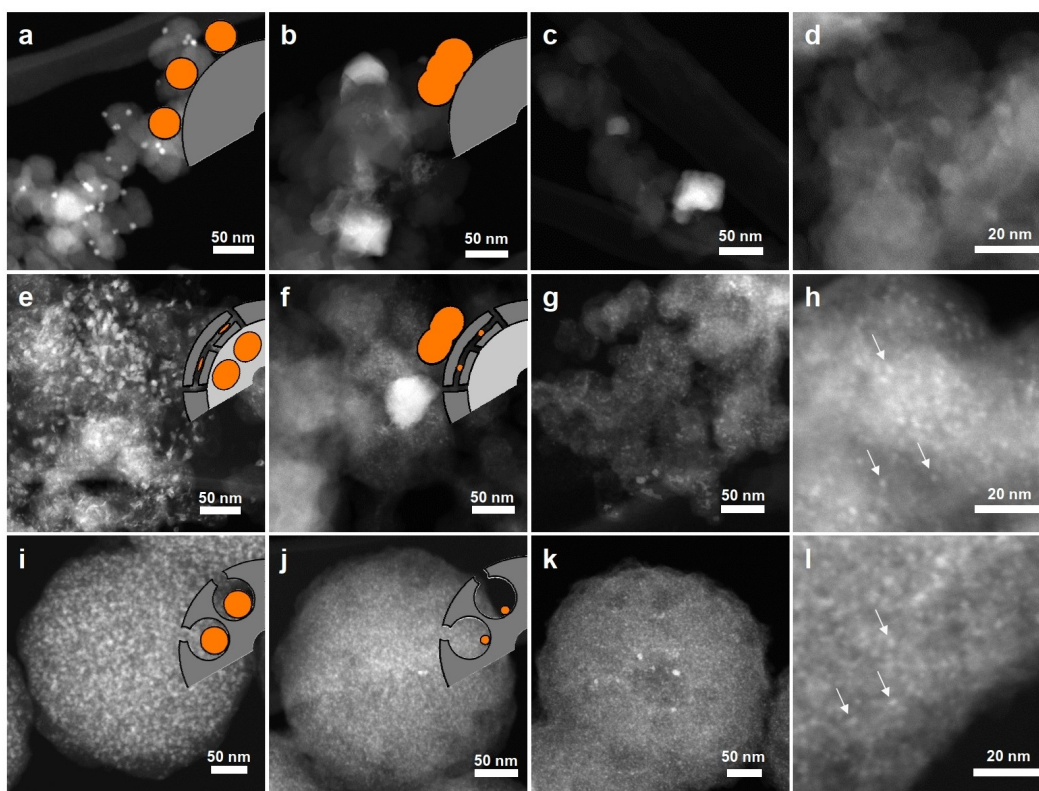


Figure 2. HAADF-STEM micrographs of synthesized catalyst Cu@Vul (a) fresh, (b) after 100 min CO₂RR and (c, d) after 20 h CO₂RR; Cu@KB (e) fresh, (f) after 100 min CO₂RR and (g, h) after 20 h CO₂RR and Cu@MGS (i) fresh, (j) after 100 min CO₂RR and (k, l) after 20 h CO₂RR. The white arrows indicate individual CuNPs.

with air.^[23] For Cu@Vul, copper oxidation is kinetically hindered by tetradecylphosphonic acid used as a capping agent during synthesis resulting in the characteristic metallic Cu (111) reflex at $2\Theta = 43.5^\circ$ (Figure 1c). Additionally, the carbon-supported systems were characterized by high-angle annular dark-field scanning transmission electron microscopy (HAADF-STEM) to determine the support morphology, particle form, and corresponding size distribution (Figure 2).

In the two-pot synthesis strategy used for Cu@Vul (Figure 2a), CuNPs were first prepared through wet chemical synthesis and subsequently supported on Vul. From HAADF-STEM images, the obtained average particle size is 7.2 ± 0.5 nm. Due to the missing pore system of Vulcan, the spherical CuNPs are located on the outer surface of the support. For the incipient wetness impregnation (IWI) method used in the case of Cu@KB and Cu@MGS, the volume of solution containing the catalyst precursor equals 90% of the measured pore volume of the carbon support and no excess solution remains outside the pore space. For Cu@KB (Figure 2e), a bimodal particle size distribution can be distinguished by HAADF-STEM namely 2.4 ± 0.4 nm and 8.2 ± 1.2 nm. By comparing bright field, dark field HAADF-STEM, and secondary electron micrographs, it is discerned if the particles are located inside or outside of the carbon structure (Figure 3). Clearly, copper nucleation and growth on the outer carbon surface can be excluded. The crystallization inside the limited pore space of the graphitic

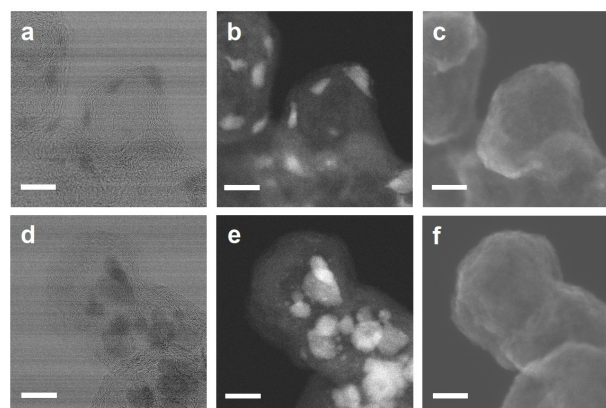


Figure 3. (a, d) Bright field, (b, e) dark field HAADF-STEM, and (c, f) secondary electron micrographs of small CuNPs (a–c) in the Ketjenblack onion-like structure and larger CuNPs (d–f) in the Ketjenblack hollow structure of the Cu@KB catalyst. Scale bar: 10 nm.

onion structure during synthesis caused the smaller 2.4 ± 0.4 nm CuNPs to exhibit an elongated particle shape, demonstrating successful impregnation (Figure 3a–c). The larger particles of 8.2 ± 1.2 nm are located in the hollow space inside the KB particles (Figure 3d–f). These different particle locations are supported by the findings of Padgett et al. in which the existence of large internal void structures and small pores in Ketjenblack are shown by low-angle annular dark-field STEM

images.^[24] As a consequence of the difficulty in detecting smaller Cu particles on STEM micrographs, the apparent ratio of smaller (< 3 nm) to larger (> 5 nm) Cu nanoparticles of 0.6 is likely greater than indicated in Figure 1e as the determined particle size distribution was made by a series of different micrographs (Figure S2). Cu@MGS (Figure 2i) contains copper particles with a unimodal particle size distribution and an approximate diameter of 4.0 ± 0.6 nm, which are uniformly distributed throughout the MGS material. Comparing the particle and pore size distribution, all particles appear to be located inside the pore system of the MGS particle.

For the first assessment of structural stability, all three catalysts were investigated on a 10 cm^2 gas diffusion electrode (GDE) and investigated in a micro-flow cell under CO_2 RR conditions. In this setup, a chronopotentiometry measurement was performed with an applied current density of $100 \text{ mA cm}_{\text{geo}}^{-2}$ for each catalyst system. To obtain an extensive overview of the stability, post-catalytic, ex-situ HAADF STEM images after 100 min and 20 h of catalysis were recorded and are shown in Figure 2. For Cu@Vul with no internal pore system and no anticipated stabilization, none of the original particles remain in their as-synthesized form after 100 min of reaction, leading to agglomerated particles with an average particle size of approximately 5 nm (Figure 2a,b). Further reaction over 100 min seems to not provoke further particle growth (Figure 2c,d). In contrast, the bimodal particle size distribution and location of CuNPs in Cu@KB resulted in two different Cu particle restructuring effects during CO_2 RR (Figure 2e–h). No agglomeration of smaller particles was detected in the Cu@KB samples after 100 min and 20 h of reaction. However, a change in the shape of these particles was seen after 100 min of reaction and the CuNPs reshaped into spherical particles of 2.5 ± 0.4 nm. This shape was retained after 20 h of reaction. After 100 min, the larger CuNPs, located in the hollow spaces of the KB material, agglomerated into larger Cu particles between 50 and 100 nm, similar to Cu@Vul. This implies that the localization of the smaller CuNPs inside the graphitic onion structure of KB either offered sufficient spatial separation or restrict the movement of the CuNPs to prevent agglomeration. This shows that a general approach to preventing agglomeration requires the consideration of both, pore confinement and pore type since pore

shape and structure essentially influence stability. In comparison, we observe no particle agglomeration for Cu@MGS after 100 min or 20 h. Similar to the small CuNP in Cu@KB, particles inside the MGS pores reduced in size to 2.4 ± 0.3 nm and retained the particle shape after 100 min up to 20 h (Figure 2i–l). In the work of Popovic et al., the reconstruction of copper is explained by a two-step dissolution and redeposition mechanism, resulting in a fragmentation of CuNPs, which could be responsible for the particle shrinkage in Cu@KB and Cu@MGS.^[14] Evidently, these results demonstrate the stabilizing effect of pore confinement on particle agglomeration during CO_2 RR over traditional nanostructured or bulk monometallic copper catalysts.

To correlate particle morphology and performance over time, the selectivity was monitored by gas chromatography (GC) as shown in Figure 4. All three systems displayed markedly different product spectra. After 100 min of reaction, Cu@Vul shows a faradaic efficiency (FE) of 48% towards CO_2 RR products and 31% H_2 production (Figure 4a). With 20% FE, ethylene is the main CO_2 RR product. Interestingly, the FE of gaseous products converges to a constant level after the first 10 min, supporting the idea of rapid reorganization in form of agglomeration in the Cu@Vul catalyst. Out of the three compared catalyst systems, Cu@KB (Figure 4b) shows the lowest CO_2 RR FE after 100 min with 42% FE towards CO_2 RR products and 34% FE towards the hydrogen evolution reaction (HER). The main CO_2 RR product for Cu@KB is CO with a FE of 21%. With 70% FE towards CO_2 RR products, the Cu@MGS system (Figure 4c) displays the highest selectivity towards CO_2 RR products and with 29% the lowest FE towards HER after 100 min of reaction. The main CO_2 RR product of Cu@MGS is methane with a FE of 42%. In contrast to Cu@Vul, both pore-confined catalyst systems showed a slower progression toward a steady state. These continuous changes in selectivity of Cu@KB and Cu@MGS over 100 min might stem from a slow but steady change in the structure of the catalyst. This sluggish change in selectivity supports the concept of particle fragmentation inside the pore system as seen in Figure 2.

The obtained selectivity seemingly contradicts previous results regarding a particle size effect and its impact on the selectivity of the electrochemical CO_2 RR.^[25] Reske et al. showed

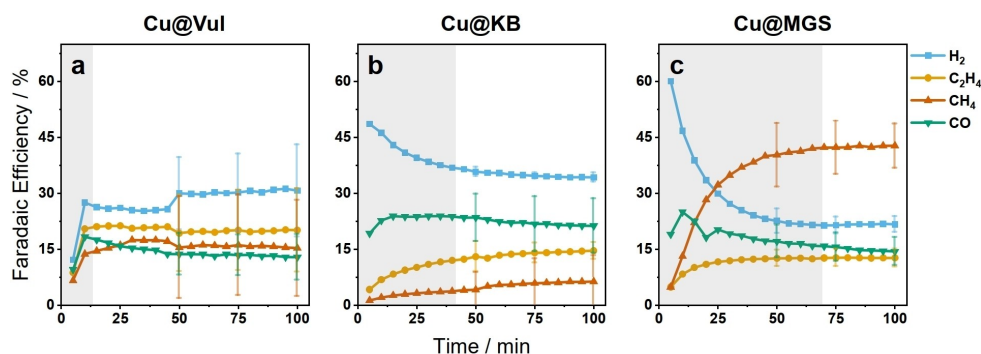


Figure 4. Faradaic efficiency of gaseous products during chronopotentiometry measurements at $100 \text{ mA cm}_{\text{geo}}^{-2}$ (10 cm^2 electrode area) in CO_2 saturated 0.5 M KHCO_3 (pH 7.2). The loadings of the three different catalysts on the GDE: (a) Cu@Vul (loading $0.5\text{--}0.6 \text{ mg cm}^{-2}$), (b) Cu@KB (loading $0.4\text{--}0.5 \text{ mg cm}^{-2}$) and (c) Cu@MGS (loading $0.1\text{--}0.2 \text{ mg cm}^{-2}$). The corresponding voltage curves are presented in Figure S4.

that smaller CuNPs in the size range of 2–15 nm displayed largely increased H₂ (60–70% compared to 20% on Cu-foil) and CO (20–25% compared to 5% on Cu-foil) FE, while the FE towards CH₄ decreased for smaller particles (10–15% compared to >55% on Cu-foil). They explained the selectivity differences by the higher share of low coordinated Cu atoms on smaller nanoparticles. Detailed post-catalytic characterization was, however, not performed. In contrast, Loiudice et al. reported increased hydrogen evolution activity for spherical, 27 nm (55% H₂), and 7.5 nm (25% H₂) large CuNPs.^[26] For the latter, post-catalytic evaluation by SEM measurements revealed significant restructuring, resulting in large agglomerates in the size range of 30–32 nm. The selectivity trend of hydrogen and CO was in line with the results previously reported by Reske et al.^[25] These results also correspond well to the observed reorganization and final selectivity of Cu@Vul. For Cu@MGS, however, agglomeration was actively prevented by pore-confinement. At the same time, the amount of CO₂RR products, especially CH₄, was high while low amounts of H₂ were observed.

Our results clearly deviate from the previously presented particle size effect and suggest that the reported particle size effect needs to be re-evaluated for the CO₂RR due to the reorganization of the catalyst. For Cu@MGS, the particle sizes decrease with time while, at the same time, the CO₂RR products increase from 29% to 70%. Similarly, for Cu@KB, the CO₂RR products increased from 25% to 42% within the first 100 min. The largest difference from previous studies lies in the support of carbon materials with unique structural elements, in which the most pronounced influence is the particular pore system of the carbon support.

To better understand the influence of the pore system on the CO₂RR product selectivity, the product spectrum was analyzed at different current densities. Figure 5 shows the FE of the three catalyst systems obtained in a GDE setup at four current densities ($j = 10, 20, 50, 100 \text{ mA cm}^{-2}$) and the representative values of iR -corrected potentials. The variation of j does not only change the applied potential but also the local pH around the catalyst through the generation of OH⁻ ions. Both, the potential and pH, influence the selectivity of the CO₂RR.^[27] Higher local pH values benefit C₂H₄ production by suppressing CH₄ and H₂ production, while not affecting the CO production as is shown for Au catalysts.^[28–30] This effect is pronounced in

porous catalyst systems in which the limited mass transport of locally generated OH⁻ inside the pore system increases the local pH more than in open systems.^[31] Additionally, an increase in applied negative potential benefits CH₄ > C₂H₄ > CO production.^[27]

At a current density of $10 \text{ mA cm}_{\text{geo}}^{-2}$ ($-0.97 \text{ V}_{\text{RHE}}$), Cu@Vul (Figure 5a) produces 7% methane. Increasing j leads to methane becoming the main CO₂RR product at $50 \text{ mA cm}_{\text{geo}}^{-2}$ ($-1.47 \text{ V}_{\text{RHE}}$) and reaching a FE of 35% at $100 \text{ mA cm}_{\text{geo}}^{-2}$ ($-1.67 \text{ V}_{\text{RHE}}$). For Cu@Vul, the FE of gaseous CO₂RR products increases from 38% at $10 \text{ mA cm}_{\text{geo}}^{-2}$ ($-0.97 \text{ V}_{\text{RHE}}$) to 46% at $100 \text{ mA cm}_{\text{geo}}^{-2}$ ($-1.67 \text{ V}_{\text{RHE}}$). In contrast, Cu@Vul shows the highest selectivity towards HER of all compared catalyst systems over the observed potential range with the H₂ FE decreasing slightly from 50% at $10 \text{ mA cm}_{\text{geo}}^{-2}$ ($-0.97 \text{ V}_{\text{RHE}}$) to 44% at $100 \text{ mA cm}_{\text{geo}}^{-2}$ ($-1.67 \text{ V}_{\text{RHE}}$). This constant HER selectivity, combined with the low C₂H₄ and high CH₄ selectivity could indicate no change in local pH.

For Cu@KB (Figure 5b), CO is the main product (50%) at a current density of $10 \text{ mA cm}_{\text{geo}}^{-2}$ ($-0.77 \text{ V}_{\text{RHE}}$). Methane and ethylene increase from 4.6% and 1.5% at $10 \text{ mA cm}_{\text{geo}}^{-2}$ ($-0.77 \text{ V}_{\text{RHE}}$) to 18.3% and 10.3% at $100 \text{ mA cm}_{\text{geo}}^{-2}$ ($-1.57 \text{ V}_{\text{RHE}}$), with ethylene becoming the main CO₂RR product at $100 \text{ mA cm}_{\text{geo}}^{-2}$. In sum, the FE towards CO₂RR products decreases from 56% at $10 \text{ mA cm}_{\text{geo}}^{-2}$ ($-0.77 \text{ V}_{\text{RHE}}$) to 44% at $100 \text{ mA cm}_{\text{geo}}^{-2}$ ($-1.57 \text{ V}_{\text{RHE}}$), with $50 \text{ mA cm}_{\text{geo}}^{-2}$ ($-1.47 \text{ V}_{\text{RHE}}$) displaying the lowest CO₂RR activity of 40% FE towards gaseous CO₂RR products. The HER activity of the catalyst decreases with increasing j from 46% at $10 \text{ mA cm}_{\text{geo}}^{-2}$ ($-0.77 \text{ V}_{\text{RHE}}$) to 35% at $100 \text{ mA cm}_{\text{geo}}^{-2}$ ($-1.57 \text{ V}_{\text{RHE}}$). These results contrast the Cu@Vul findings. The overall change in FE with j indicates a local pH increase, which might stem from the pore confinement of copper catalyst nanoparticles in the carbon matrix.

Similar to Cu@KB the main product of Cu@MGS (Figure 5c) at $10 \text{ mA cm}_{\text{geo}}^{-2}$ ($-0.97 \text{ V}_{\text{RHE}}$) is CO with a FE of 49%. The selectivity for ethylene and methane increases from 10 to $100 \text{ mA cm}_{\text{geo}}^{-2}$ ($-1.32 \text{ V}_{\text{RHE}}$), with methane becoming the main CO₂RR product (29%) at $50 \text{ mA cm}_{\text{geo}}^{-2}$ ($-1.29 \text{ V}_{\text{RHE}}$) and the main product of the catalyst (50%) at $100 \text{ mA cm}_{\text{geo}}^{-2}$ ($-1.32 \text{ V}_{\text{RHE}}$). Cu@MGS suppresses the undesired HER drastically over the entire potential range reported, ranging from 43% at $10 \text{ mA cm}_{\text{geo}}^{-2}$ ($-0.97 \text{ V}_{\text{RHE}}$) to 36% at $50 \text{ mA cm}_{\text{geo}}^{-2}$ ($-1.29 \text{ V}_{\text{RHE}}$)

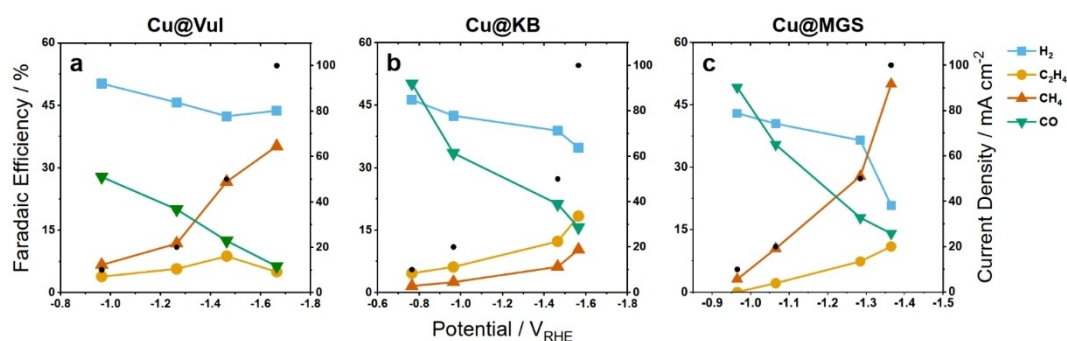


Figure 5. Faradaic efficiency of gaseous products vs. corresponding iR corrected potential at 10, 20, 50, and $100 \text{ mA cm}_{\text{geo}}^{-2}$ for (a) Cu@Vul, (b) Cu@KB and (c) Cu@MGS. Black dots represent the corresponding current density for each step (right y-axis).

and significantly decreasing to 21% at 100 mA cm_{geo}⁻² (-1.32 V_{RHE}). Additional to the low unfavorable HER activity, Cu@MGS displays the highest FE of gaseous CO₂RR of all investigated catalyst systems with a CO₂RR FE of 52% at 10 mA cm_{geo}⁻² (-0.97 V_{RHE}) up to 75% at 100 mA cm_{geo}⁻² (-1.32 V_{RHE}). With the increase of C₂H₄ and the significant decrease of H₂ with higher current densities, the results of Cu@MGS also point towards the increase of the local pH. This is not reflected in the simultaneous increase of the main product CH₄ and suggests the influence of different effects such as retention time, mass transport limitations, or substrate effects. Clearly, an effect of pore confinement on selectivity can be observed and further studies have to reveal the full picture to correlate pore confinement and selectivity.

Conclusion

In this work, we investigated the influence of the carbon support pore structure on the reorganization behavior of CuNPs during the CO₂RR. By precisely controlling the synthesis conditions, three representative catalytic materials were prepared by wet synthesis and incipient wetness impregnation methods and were tested in a micro-flow cell with online analytics. Pre- and post-catalytic HAADF-STEM measurements revealed the ability of pore confinement to impede particle coalescence and agglomeration. Stabilization arises from the spatial separation and confinement of CuNPs within the pore structure. Non-stabilized CuNPs demonstrate a drastic reorganization that predominantly takes place when the particles are not located in a stabilizing pore structure. Preventing agglomeration opens up the possibility to investigate particle fragmentation without overlaying reorganization effects by in-situ morphological or electrolyte studies to precisely understand the progression of particle shrinkage during the CO₂RR. Intriguingly, a high share of CO₂RR products was observed for stabilized nanoparticles in MGS questioning the established particle size effect for the CO₂RR, where H₂ was predominantly observed on nanoparticles below 15 nm. Our findings open new ways of stabilizing copper nanoparticles and demonstrate the necessity of post-catalytic assessment of the catalysts' morphological state to precisely derive performance-structure indicators. These results lay the foundation for future work on tuning the stability and selectivity of copper catalysts through the incorporation into a suitable support pore system.

Experimental Section

MGS synthesis

The chemical vapor deposition (CVD) synthesis of the mesoporous graphitic spheres was carried out as reported by Knossalla et al.^[22] For the synthesis of the SiO₂ hard template 450 mL of ethanol, 72 mL of water, and 17.4 mL of 25 wt.% ammonium hydroxide solution was mixed. The mixture was stirred for 15 min, after which 15 mL of tetraethylorthosilicate (TEOS) and 6 mL of octadecyltrimethoxysilane (OTMS) were added under rapid stirring.

After further stirring overnight, the suspension was centrifuged and the collected solid dried at 75 °C overnight. The dry material was subsequently calcined in air with a heating rate of 1 K min⁻¹ and held for 3 h at a temperature of 550 °C. The resulting material was ground with a mortar and pestle. To obtain the MGS, 2 g of the SiO₂ template and 10 g ferrocene were placed in two separate quartz crucibles inside a quartz tube. The tube was then placed inside a tubular furnace and heated with a heating rate of 5 K min⁻¹ to 550 °C in an argon flow of 100 mL min⁻¹. Here the crucible containing the silica template was centered in the heating zone of the furnace. Once the tubular furnace reached 500 °C a heating jacket at the quartz tube inlet was heated to 140 °C. The ferrocene-containing crucible was centered in the heating zone of the heating jacket. After 1.5 h of dwelling time, the heating jacket and furnace were switched off and cooled down to ambient temperature, while Ar flow was maintained. Before the material was collected the sample was passivated by an O₂/N₂ (1:99 Vol.%) flow of 100 mL min⁻¹ for 1.5 h, otherwise, the sample would spontaneously ignite in contact with air. After this, the material was carbonized at 800 °C for 4 h in an argon flow of 100 mL min⁻¹. The remaining silica was leached by HF. Typically, 1 g of the resulting composite was submerged in 7 mL of 40% HF for 24 h and subsequently washed with water. Following this step, iron was leached from the material using 7 mL of 30% HCl per g of composite material and stirred at 60 °C overnight. Consecutively the resulting material was washed with water and dried at 80 °C overnight.

Wet synthesis of Cu@Vul

Size-controlled CuNPs of roughly 7 nm were prepared according to a literature procedure by Osowecki et al.^[19] For this, trioctylamine (Sigma-Aldrich, 98%) was degassed in a Schlenk flask for one hour (90 °C, vacuum). Under Schlenk conditions, 202.5 mg of copper(I) acetate (Sigma-Aldrich, 97%), 226.3 mg of n-tetradecylphosphonic acid (Sigma-Aldrich, 98%), and 16.3 mL of the degassed trioctylamine were added to a 25 mL three-neck flask. The solution was then stirred and heated to 105 °C under an argon atmosphere to ensure the complete dissolution of solids. Subsequently, the mixture was heated rapidly (2 K s⁻¹) to 180 °C, held for 30 min at this temperature, again heated rapidly (2 K s⁻¹) to 270 °C and kept at this temperature for 30 min. After the purplish-red solution was cooled down to room temperature, the Cu particles were precipitated by the addition of a 3:1 ethanol:isopropanol (technical grade) mixture (1.25 × the volume of the trioctylamine solution) and centrifuged at 6,500 rpm for 5 minutes. After cleaning, the CuNPs were redispersed in hexane and cleaned one more time. Subsequently, the CuNPs were redispersed in hexane as 900 mg Vulcan XC72R was added to the dispersion. The mixture was then ultrasonicated for 30 min and centrifuged at 6,500 rpm for 5 minutes. Subsequently, the mixture was dried at room temperature and the final catalyst was collected.

Incipient-wetness-synthesis

In the first step of the incipient wetness impregnation, the carbon material was dried. For this, the carbon material and a stirring bar were added to a round flask, and vacuum was applied. The temperature of an oil bath was slowly increased (20 °C/30 minutes) to avoid the carbon material to burst into the piping. After reaching 150 °C the temperature was held for 60 min. Following this, the carbon material was cooled down to room temperature. In the second step, the impregnation of the carbon material was done. For this, 90% of the calculated pore volume was used as the volume of the impregnation solution. The concentration of the impregnation solution was then calculated based on available pore

volume and desired loading. For this, the $\text{CuNO}_3 \cdot 3\text{H}_2\text{O}$ (Honeywell Fluka, 99–104%) precursor was dissolved in 1 M HNO_3 . The clear solution was filtered through a syringe filter to prevent undissolved particles in the impregnation solution. Subsequently, the filtered solution was applied to the carbon material under strong stirring in three equally sized portions. To ensure uniform pore filling, the round flask was put into the ultrasonic bath for 30 minutes. The mixture was then dried in vacuum at room temperature overnight. In the final step, the mixture is calcined in a tube furnace with a gas flow of 10 NL h^{-1} 20% H_2 in N_2 . The oven was heated with a heating rate of 2 K min^{-1} until it reached 230°C , which was held for 30 minutes. Subsequently, the H_2 gas flow was stopped and the oven was naturally cooled down to ambient temperatures under a N_2 flow (8 NL h^{-1}).

Fabrication of gas diffusion electrodes

The fabrication of gas diffusion electrodes is carried out by airbrushing a catalyst ink on a commercial carbon-based gas diffusion layer (Sigracet 39BC). The ink contains around 15 mg of the respective catalyst powder, 5 mg of Nafion solution (5 wt.%), and 10 g of isopropanol. After ultrasonication for 10 min, the ink is manually sprayed on the gas diffusion layer which is heated up to 100°C by a heating plate. The loading is crosschecked by weighing: Cu@KB: $0.4\text{--}0.5 \text{ mg cm}^{-2}$; Cu@Vulcan: $0.5\text{--}0.6 \text{ mg cm}^{-2}$; Cu@MGS: $0.1\text{--}0.2 \text{ mg cm}^{-2}$.

Electrochemical measurement of catalyst

Electrochemical characterization is carried out in a commercial micro-flow cell (Electrocell®). The cell consists of anode and cathode compartments, which are continuously fed by a peristaltic pump and separated by an anion exchange membrane (fumasep® FAS-50, Fumatech). 0.5 M KHCO_3 is used as electrolyte [Potassium bicarbonate (VWR) and ultrapure water (18 M Ω , Elga)] in both compartments. The active area of the gas diffusion electrode is 10 cm^2 . A platinum-coated titanium plate and an ET072 leakless miniature Ag/AgCl reference electrode are used as anode and reference electrode, respectively. The outlet of the CO_2 stream (Linde, grade 4.5) (90 mL min^{-1}) is analyzed via gas chromatography every 5 min (Micro GC 490, Agilent.)

Acknowledgements

EK thanks the Deutsche Forschungsgemeinschaft (DFG) for financial support (FK: 511462370). ML acknowledges the Federal Ministry of Education and Research (BMBF) in the framework of NanoMatFutur (SynKat, FK: 03XP0265) for financial support. A.G. acknowledges the support of the IMPRS-SurMat doctoral program. A.G., F.S., T.I., and P.P. acknowledge the Federal Ministry for Economic Affairs and Energy (BMWi) of Germany in the framework of POREForm (project number 03ETB027F and 03ETB027G). M.L. and B.E. acknowledge the "Dr. Illing Stiftung für makromolekulare und angewandte Chemie" for support. Open Access funding enabled and organized by Projekt DEAL.

Conflict of Interest

The authors declare no conflict of interest.

Data Availability Statement

The data that support the findings of this study are available from the corresponding author upon reasonable request.

Keywords: copper · electrochemical CO_2 reduction · pore confinement · stability · supported catalyst

- [1] IPCC, *Summary for Policymakers. In: Climate Change 2021: The Physical Science Basis. Contribution of Working Group I to the Sixth Assessment Report of the Intergovernmental Panel on Climate Change*, Cambridge University Press. In Press, 2021, SPM-9.
- [2] Y. Hori, *Modern Aspects of Electrochemistry No. 42*, Springer, 2008.
- [3] K. P. Kuhl, E. R. Cave, D. N. Abram, T. F. Jaramillo, *Energy Environ. Sci.* 2012, 5, 7050–7059.
- [4] S. Nitopi, E. Bertheussen, S. B. Scott, X. Liu, A. K. Engstfeld, S. Horch, B. Seger, I. E. L. Stephens, K. Chan, C. Hahn, J. K. Nørskov, T. F. Jaramillo, I. Chorkendorff, *Chem. Rev.* 2019, 119, 7610–7672.
- [5] D. Kim, C. S. Kley, Y. Li, P. Yang, *Proc. Natl. Acad. Sci. USA* 2017, 114, 10560–10565.
- [6] Y. Li, F. Cui, M. B. Ross, D. Kim, Y. Sun, P. Yang, *Nano Lett.* 2017, 17, 1312–1317.
- [7] Z. Wang, G. Yang, Z. Zhang, M. Jin, Y. Yin, *ACS Nano* 2016, 10, 4559–4564.
- [8] J. Yuan, J. J. Zhang, M. P. Yang, W. J. Meng, H. Wang, J. X. Lu, *Catalysts* 2018, 8, 171–181.
- [9] K. Gupta, M. Bersani, J. A. Darr, *J. Mater. Chem. A* 2016, 4, 13786–13794.
- [10] Q. Lei, H. Zhu, K. Song, N. Wei, L. Liu, D. Zhang, J. Yin, X. Dong, K. Yao, N. Wang, X. Li, B. Davaasuren, J. Wang, Y. Han, *J. Am. Chem. Soc.* 2020, 142, 4213–4222.
- [11] K. D. Yang, W. R. Ko, J. H. Lee, S. J. Kim, H. Lee, M. H. Lee, K. T. Nam, *Angew. Chem. Int. Ed.* 2017, 56, 796–800; *Angew. Chem.* 2017, 129, 814–818.
- [12] C. G. Morales-Guio, E. R. Cave, S. A. Nitopi, J. T. Feaster, L. Wang, K. P. Kuhl, A. Jackson, N. C. Johnson, D. N. Abram, T. Hatsukade, C. Hahn, T. F. Jaramillo, *Nat. Catal.* 2018, 1, 764–771.
- [13] G. R. Zhang, S. D. Straub, L. L. Shen, Y. Hermans, P. Schmatz, A. M. Reichert, J. P. Hofmann, I. Katsounaros, B. J. M. Etzold, *Angew. Chem. Int. Ed.* 2020, 59, 18095–18102; *Angew. Chem.* 2020, 132, 18251–18258.
- [14] S. Popovic, M. Bele, N. Hodnik, *ChemElectroChem* 2021, 8, 2634–2639.
- [15] J. Vavra, T. H. Shen, D. Stoian, V. Tileli, R. Buonsanti, *Angew. Chem. Int. Ed.* 2021, 60, 1347–1354; *Angew. Chem.* 2021, 133, 1367–1374.
- [16] Y. G. Kim, J. H. Baricuatro, A. Javier, J. M. Gregoire, M. P. Soriaga, *Langmuir* 2014, 30, 15053–15056.
- [17] R. M. Arán-Ais, R. Rizo, P. Grosse, G. Algara-Siller, K. Dembélé, M. Plodinec, T. Lunkenbein, S. W. Chee, B. R. Cuenya, *Nat. Commun.* 2020, 11 (1–8), 3489.
- [18] J. Huang, N. Hörmann, E. Oveisi, A. Louidice, G. L. De Gregorio, O. Andreussi, N. Marzari, R. Buonsanti, *Nat. Commun.* 2018, 9, 1–9.
- [19] W. T. Osowiecki, J. J. Nussbaum, G. A. Kamat, G. Katsoukis, M. Ledendecker, H. Frei, A. T. Bell, A. P. Alivisatos, *ACS Appl. Energ. Mater.* 2019, 2, 7744–7749.
- [20] A. V. Neimark, Y. Lin, P. I. Ravikovitch, M. Thommes, *Carbon* 2009, 47, 1617–1628.
- [21] M. Thommes, K. Kaneko, A. V. Neimark, J. P. Olivier, F. Rodriguez-Reinoso, J. Rouquerol, K. S. W. Sing, *Pure Appl. Chem.* 2015, 87, 1051–1069.
- [22] J. Knossalla, J. Mielby, D. Göhl, F. R. Wang, D. Jalalpoor, A. Hopf, K. J. J. Mayrhofer, M. Ledendecker, F. Schüth, *ACS Appl. Energ. Mater.* 2021, 4, 5840–5847.
- [23] C. H. Chen, T. Yamaguchi, K. I. Sugawara, K. Koga, *J. Phys. Chem. B* 2005, 109, 20669–20672.
- [24] E. Padgett, N. Andrejevic, Z. Liu, A. Kongkanand, W. Gu, K. Moriyama, Y. Jiang, S. Kumaraguru, T. E. Moylan, R. Kukreja, D. A. Muller, *J. Electrochem. Soc.* 2018, 165, F173–F180.
- [25] R. Reske, H. Mistry, F. Behafarid, B. Roldan Cuenya, P. Strasser, *J. Am. Chem. Soc.* 2014, 136, 6978–6986.
- [26] A. Louidice, P. Lobaccaro, E. A. Kamali, T. Thao, B. H. Huang, J. W. Ager, R. Buonsanti, *Angew. Chem. Int. Ed.* 2016, 55, 5789–5792; *Angew. Chem.* 2016, 128, 5883–5886.
- [27] D. Ren, J. Fong, B. S. Yeo, *Nat. Commun.* 2018, 9, 925.

- [28] K. J. P. Schouten, E. Pérez Gallent, M. T. M. Koper, *J. Electroanal. Chem.* **2014**, *716*, 53–57.
- [29] S. Ringe, C. G. Morales-Guio, L. D. Chen, M. Fields, T. F. Jaramillo, C. Hahn, K. Chan, *Nat. Commun.* **2020**, *11*, 33.
- [30] A. S. Varela, *Curr. Opin. Green Sustain. Chem.* **2020**, *26*, 100371.
- [31] A. Goyal, C. J. Bondue, M. Graf, M. T. M. Koper, *Chem. Sci.* **2022**, *13*, 3288–3298.

Manuscript received: September 15, 2022
Revised manuscript received: November 2, 2022
Version of record online: January 3, 2023